Electronic transport in quantum cascade structures at equilibrium

C. Koeniguer, G. Dubois,[*] A. Gomez, and V. Berger

Matériaux et Phénomènes Quantiques, Université Paris 7, Case 7021, 2 Pl Jussieu, 75251 Paris, France

The transport in complex multiple quantum well heterostructures is theoretically described. The model is focused on quantum cascade detectors, which represent an exciting challenge due to the complexity of the structure containing seven or eight quantum wells of different widths. Electronic transport can be fully described without any other adjustable parameter than the doping density. Diffusion from one subband to another is calculated with a standard electron-optical phonon Hamiltonian, and the electronic transport results from a parallel flow of electrons using all the possible paths through the different subbands. Finally, the resistance of such a complex device is given by a simple expression, with an excellent agreement with experimental results. This relation involves the sum of transitions rates between subbands, from one period of the device to the next one. This relation appears as an Einstein relation adapted to the case of complex multiple quantum structures.

I. INTRODUCTION

Quantum well infrared photodetectors (QWIPs) have become widely used quantum heterostructures for thermal imaging application during the last ten years.[1] Thanks to the very recent introduction of quantum cascade detectors (QCDs),[2–4] QWIPs exist now in two modes of electronic transport: photoconductive and photovoltaic. For the first type (the regular QWIP inserted today in focal plane arrays), an external bias is necessary to drift the electrons. They are characterized by a dark current and so they operate at low temperature. The second type of detectors uses a photovoltaic mode: no external bias is applied. No dark current exists in these devices and they are promising for applications at higher temperature, larger wavelengths,[3] and smaller pixel areas. In all these structures, however, the electronic transport is a very complex issue and the performances of the devices are finally governed by fundamental physics problems.

In a standard QWIP, the transport involves both two-dimensional (2D) and 3D electronic states in the quantum well and in the continuum, respectively. The diffusion of electrons from 3D to 2D states (and vice versa) is a particularly difficult theoretical problem.[5,6] That is why most models use adjustable parameters such as the capture time[7] or the capture probability, affecting the photoconductive gain.[8] In quantum cascade lasers, on another side, significant electric fields are applied, resulting in charge transfers. The description of the electronic transport has to involve Schrödinger and Poisson equations self-consistantly, which is a source of difficulty as well. Quantum cascade devices have been described with kinetic model band making use the Monte Carlo simulation.[9] With respect to these two devices, the QCD structure is rather simple since it involves only 2D states (and therefore matrix elements can be calculated without difficulty) and no bias is applied: there is no need for the Poisson equation, and the flat band condition is an excellent approximation, also because the doping levels are low. For all these reasons, the QCD appears as an archetype of complex quantum heterostructures, a model system for the experimental study of the electronic transport in a complex multiple

quantum well structure at equilibrium together with its modeling. This will be shown in this paper, in which the mechanisms of electronic transport in quantum cascade detectors are described. Electronic transport in such a complex structure is calculated without any other adjustable parameters than the doping density, and also standard effective masses and band offsets found in the general literature on semiconductors. The details of the QCD structure and the principle of detection are described in Sec. II. In Sec. III, the model describing the electronic transport is presented in details, relying on the calculation of all the transition rates between different subbands due to an electron-optical phonon Hamiltonian. Through an analytical derivation of the sum of the different paths that an electron can follow to cross the structure, the resistance of the complex multiple quantum well structure is expressed in a very simple form (Sec. IV). The analogy between this expression and the Einstein relation will be underlined.

II. PRESENTATION OF A QUANTUM CASCADE DETECTOR

The QCD considered in this paper is a GaAs/AlGaAs heterostructure composed of 40 periods of seven quantum wells. The quantum wells are made in GaAs. The first quantum well of each period is n doped in order to populate its first energy level E_1 in the conduction band with electrons (the nominal doping concentration is about 5×10^{11} cm^{-2}). Barriers are made in Al$_{0.34}$GaAs$_{0.66}$. The quantum wells (respectively, the barriers) have the following widths: 68, 20, 23, 28, 34, 39, and 48 Å (respectively, 56.5, 39.55, 31, 31, 31, 31, 22.6 Å). These dimensions have been optimized in order to create the quantum cascade of levels shown in Fig. 1. Figure 1(a) presents wave functions associated with each energy subband, in one period of the device. The envelope functions have been calculated with a 1D Schrödinger equation in a single band approximation. Space charge effects have been neglected. We have indeed verify that a self-consistent calculation does not change the result significantly, since all the electrons and the Si donors are located in the fundamental level. Wave functions associated with each
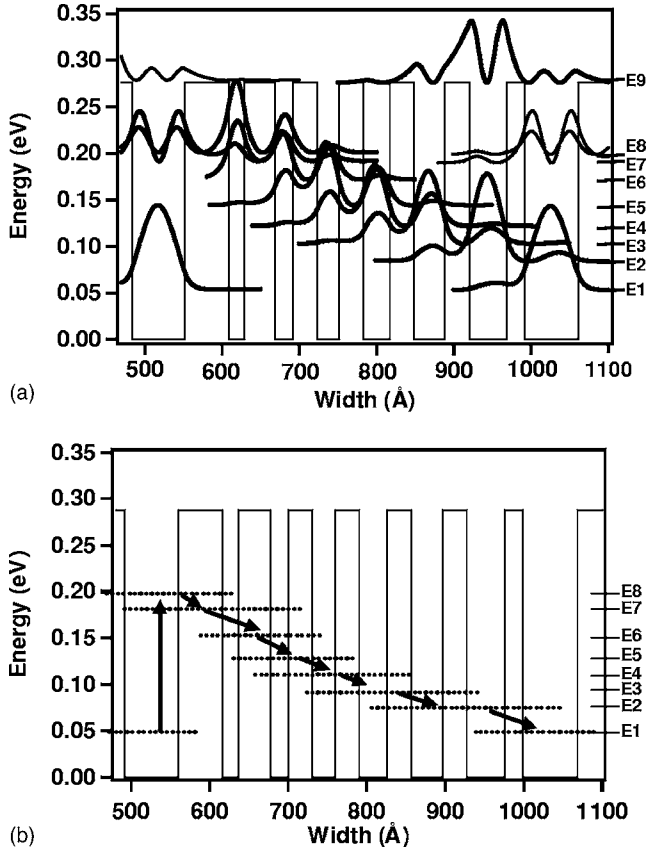
FIG. 1. Presentation of a period of a QCD. (a) Conduction band diagram and wave function associated with each energy level of a period. (b) Principle of a detection.

energy subband are delocalized through the heterostructure. Absorption of a photon brings electrons from the first energy level to energy E_7 or E_8. The first and the second quantum wells are coupled. In this way, electrons are transferred from level E_7 or E_8 towards energy level E_6 mostly through the longitudinal optical phonon interaction. Because of the coupling between the second and the third quantum well, electrons will be relaxed to energy level E_5 and so on. Electrons are relaxing from the left to the right of the structure step by step [see Fig. 1(b)]. Finally the net result under illumination is the transfer of electrons from energy level E_1 of one period to energy level E_1 of the following period. In this way, the structure acts as a photovoltaic infrared detector.

III. MODEL OF THE ELECTRONIC TRANSPORT

As usual with this kind of device, the resistance will be presented in terms of $R_0 A$ (where R_0 is the resistance of the pixel and A the area of the pixel). Hypotheses about electronic transitions between the different energy levels have to be made for the determination of the $R_0 A$ of such a structure. Considering the well and barrier widths, only interactions between electrons and optical phonons (LO phonons) have been taken into account. The differences between the energy levels are indeed sufficiently high to neglect the influence of the interaction between electrons and acoustical phonons.[10]

All other possible interactions have been neglected, too. Interface roughness has low influence on intersubband scattering, although it was possible to measure its influence at very low temperature[11] (4 K). Electron-electron interaction is efficient for electrons thermalization inside a subband,[12,13] but negligible for intersubband scattering in our cascade scheme with many subband separations greater than 36 meV which corresponds to the energy of the optical phonons[14,15] (acoustical phonons and carrier-carrier interactions are implicitly taken into account in our model when we assume an electronic population at thermal equilibrium since the thermalization is mediated through these interactions, but optical phonons are the only interaction considered for the description of transitions rates between two differents subbands). The transition rates due to the interaction between electrons and optical phonons will be evaluated first following Ferreira and Bastard.[16] Bulk phonons have been used in the calculation. Starting from an initial state of wave vector k and energy E in the subband i, the transition rate $S_{ij}^{a,e}(E)$ towards the subband j (in s^{-1}) is obtained through the integration of a matrix element involving a standard electron-optical-phonon Hamiltonian. This integration involves all the possible final states of energy $E \pm \hbar \omega_{LO}$ in the subband j, where ω_{LO} is the energy of a LO phonon, the plus or minus sign accounting for absorption or emission of LO phonons, corresponding to superscript a or e, respectively. This evaluation is made in the parabolic approximation of the energy bands (our structures use low Aluminum content AlGaAs barriers, and low energy levels because of the detection wavelength which is greater than 8 μm). Transitions rates S_{ij}^a and S_{ji}^e are linked by the following equation:

$$S_{ij}^a(E) = S_{ji}^e(E + \hbar \omega_{LO}). \quad (1)$$

Finally, the global transition rate G_{ij} between the subband i and subband j is the sum of the two transition rates for absorption of LO phonons (G_{ij}^a), and emission of LO phonons (G_{ij}^e). In order to calculate the global transition rates G_{ij}^a and G_{ij}^e, all the initial states of energy E are filled at thermal equilibrium by the Fermi-Dirac occupation factor f. A single electronic temperature is assumed for all subbands and equal to the temperature of the lattice. Let us first consider the electronic promotion from a subband i to a higher subband j (i.e., $j > i$). The integration on all these states is now performed on the subband i:

$$G_{ij}^a = \int_{\epsilon_j - \hbar \omega_{LO}}^{+\infty} S_{ij}^a(E) f(E)[1 - f(E + \hbar \omega_{LO})] n_{opt} D(E) dE,$$

$$(2)$$

$$G_{ij}^e = \int_{\epsilon_j + \hbar \omega_{LO}}^{+\infty} S_{ij}^e(E) f(E)[1 - f(E - \hbar \omega_{LO})]$$
$$\times (1 + n_{opt}) D(E) dE; \quad (3)$$

n_{opt} is the Bose-Einstein statistic function which accounts for phonon population, $D(E)$ the two-dimensional density of states of the subband i and ϵ_j is the minimum of energy of the subband j. Of course, similar expressions can be written in the case of electronic transfers from a subband i to a lower
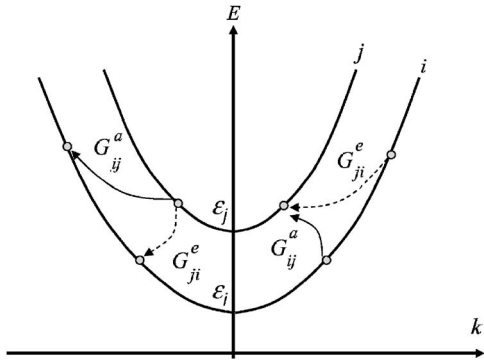
FIG. 2. The different types of electronic transitions between two subbands i and j.

subband j. Figure 2 summarizes the four possible electronic transitions.

At thermodynamical equilibrium, each global coefficient G_{ij} is equal to its reciprocal factor G_{ji}. The number of electrons per second transferred from subband i to subband j is equal to the number of electrons per second transferred back from subband j to subband i. The net current is null and the population in every subband is stationary.

In the context of a photovoltaic detector, the resistance at 0 V is a key parameter since it governs the Johnson noise of the device. The calculation of this resistance needs the determination of the current for a very small applied bias. The bias can then be introduced as a perturbation, and therefore we will suppose that the matrix elements and the $S_{ij}(E)$ transition rates do not depend on the voltage. Indeed, the elec-

tronic wave functions given by the weakly perturbed potential can be supposed nondependant on the arbitrary small voltage. In the frame of this approximation, the current results only from the variation with the applied bias of the distribution of the population as a function of the energy which affect the $G_{ij}s$ through the occupation factors f.

As an illustration of the exchanges of electrons between subbands occurring in the structure, Fig. 3 represents the main transition rates at thermodynamical equilibrium at 80 K. In addition, these transfer rates are indicated in Table I. Transition times τ_{ij} can be deduced from the global transition rate G_{ij} by

$$\tau_{ij} = n_i/G_{ij}, \qquad (4)$$

where n_i is the two-dimensional carrier density associated with the subband i. Two consecutive cascades A and B are represented in Fig. 3. For sake of clarity, transitions between two levels in the same cascade have been represented separately from transitions between two levels in consecutive cascades. In Fig. 3(a), most significant intracascade transitions are represented. The typical value of transitions rates between two neighboring levels are between a few 10^{20} and 10^{25} m^{-2} s^{-1}, corresponding to transition times between a few ps and a few tens of ps for a temperature of 80 K. In Fig. 3(b), the intercascade transitions are reported. Again, the solid-line arrows represent the main transfer rates between one cascade and the following one, but these transitions are now limited to a few 10^{18} m^{-2} s^{-1} at the same temperature (and a corresponding transition time greater than 1 μs due also to the low amount of electron promotion to higher sub-
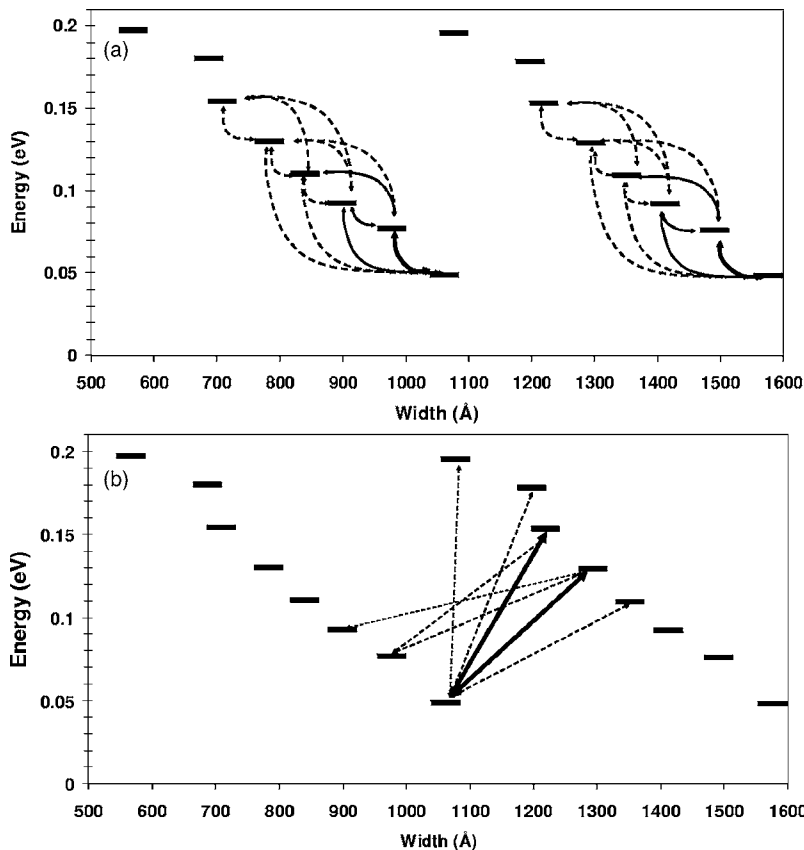

FIG. 3. Major transition rates of two consecutive cascades of the real device at 80 K. (a) The main transition rates inside each cascade (only the transition rates greater than 10^{20} m^{-2} s^{-1} are represented). (b) The main transitions between the cascades: solid lines concern the major transition (greater than 4×10^{18} m^{-2} s^{-1}), whereas dashed lines represents the other main transitions (greater than 1×10^{18} m^{-2} s^{-1} and lower than the major transitions).

TABLE I. Values of some transition rates in relation to the main electronic transition represented on Fig. 3. The left column concerns the higher transition rates inside each cascade (intracascade transition rate) and the right column gives the higher transition rates between two consecutive cascades (intercascade transitions rates). These values are evaluated at 80 K.

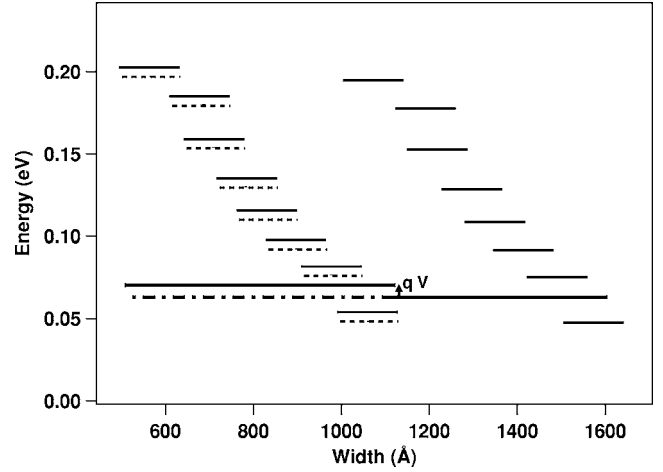| Intracascade transition rate ($m^{-2}\,s^{-1}$)	Intercascade transition rate ($m^{-2}\,s^{-1}$)
$G_{12}=2.7\times10^{25}$	$G_{14}=3.0\times10^{18}$
$G_{13}=1.0\times10^{24}$	$G_{15}=5.1\times10^{18}$
$G_{14}=1.2\times10^{22}$	$G_{16}=5.0\times10^{18}$
$G_{23}=1.7\times10^{24}$	$G_{17}=3.5\times10^{18}$
$G_{24}=3.8\times10^{23}$	$G_{18}=2.3\times10^{18}$
$G_{25}=1.2\times10^{21}$	$G_{24}=1.1\times10^{18}$
$G_{34}=1.9\times10^{23}$	$G_{25}=4.6\times10^{18}$
$G_{35}=2.2\times10^{22}$	$G_{26}=1.3\times10^{18}$
$G_{45}=1.2\times10^{22}$	$G_{35}=1.3\times10^{18}$
$G_{56}=4.6\times10^{20}$	

FIG. 4. Evolution of the first cascade in relation to the second cascade under a bias voltage. Solid lines represent the position of the energy levels under a bias voltage and dashed lines concern the position of the energy levels without any applied voltage. Fermi levels are represented on this figure in bold lines.

bands for satisfying the Fermi-Dirac distribution). The dashed-line arrows represent other minor transitions. The comparison between intra- and intercascade transitions shows that the electronic mobility is higher inside a cascade than between two consecutive cascades by several orders of magnitude. This justifies our classification between inter- and intracascade transitions and has major consequences on the understanding of the transport in the structure. It recalls the situation in a *p-n* junction, where intraband thermalization is faster than interband recombination by several orders of magnitude (picoseconds versus nanoseconds). More generally, this is a very general situation in the physics of transport where a system can be divided into two reservoirs separated by a bottleneck for the conduction. The concept of quasi-Fermi level can be imported from the *p-n* junction formalism into our case. Each cascade stays at a quasithermodynamical equilibrium. Two quasi-Fermi levels associated with two consecutive cascades can be considered: the cascade *A* (respectively *B*) is associated with the quasi-Fermi energy E_F^A (respectively E_F^B). At thermodynamical equilibrium without applying any voltage these two quasi-Fermi levels are equal. The structure is characterized by only one Fermi level. In the presence of an external applied voltage, a gap between the two quasi-Fermi levels appears and increases with the voltage: $E_F^A=E_F^B+qV$. Each energy level of the cascade *A* increases of the same factor qV, too. Figure 4 represents the situation of two consecutive cascades under a bias voltage *V*.

The main transitions at 80 K between two consecutive cascades occur between subband E_1^A to the subbands E_5^B and E_6^B (transition towards level E_5^B is more efficient than the other transitions). In conclusion, the resistance of a QCD is completely determined at 80 K by a few intercascade cross transitions, namely $E_1^A \rightarrow E_5^B$ and $E_1^A \rightarrow E_6^B$. The optimization of a QCD requires decreasing these transitions rates, thus increasing the resistance and decreasing the noise figure. This is possible by a separation of the wave functions, but at the expanse of a lower optical matrix element, and a lower response. All the challenge of the QCD design consists of mastering this trade off.

IV. DERIVATION OF AN EINSTEIN RELATION

The global current density will be evaluated by counting the electronic transitions between the two consecutive cascades. On one hand, each cascade stays at thermodynamical equilibrium, but on the other hand equilibrium between the two consecutives cascade is broken. As a consequence, transition rates from cascade *A* to cascade *B* are not equal to the reciprocal transitions rates from cascade *B* to cascade *A*. A global current appears. This global current density is given by

$$J=q\sum_{i\in A}\sum_{j\in B}[G_{ij}(V)-G_{ji}(V)]. \tag{5}$$

Let us consider two subbands *i* and *j* associated, respectively, with cascades *A* and *B*. The introduction of two quasi-Fermi levels implies the differentiation of the two Fermi occupation factors in Eq. (2) and Eq. (3). G_{ij}^a and G_{ji}^e can be evaluated by

$$G_{ij}^a(V)=\int_{\epsilon_j-\hbar\omega_{LO}}^{+\infty}S_{ij}^a(E)f_A(E)[1-f_B(E+\hbar\,\omega_{LO})]$$
$$\times n_{opt}D(E)dE, \tag{6}$$

$$G_{ji}^e(V)=\int_{\epsilon_j}^{+\infty}S_{ji}^e(E)f_B(E)[1-f_A(E-\hbar\,\omega_{LO})]$$
$$\times(1+n_{opt})D(E)dE, \tag{7}$$

where f_A and f_B are the Fermi-Dirac occupation factors associated with quasi-Fermi level E_F^A and E_F^B. Considering Eq. (1), the difference is then equal to

$$G_{ij}^{a}(V) - G_{ji}^{e}(V) = \int_{\epsilon_j - \hbar\omega_{LO}}^{+\infty} S_{ij}^{a}(E)\alpha(E)[1 - \gamma(E)]dE, \quad (8)$$

where

$$\alpha(E) = n_{opt}f_A(E)[1 - f_B(E + \hbar\,\omega_{LO})]D(E), \quad (9)$$

$$\gamma(E) = \frac{f_B(E + \hbar\,\omega_{LO})[1 - f_A(E)](1 + n_{opt})}{f_A(E)[1 - f_B(E + \hbar\,\omega_{LO})]n_{opt}}. \quad (10)$$

Without any applied voltage, the term $\alpha(E)$ is equal to $\alpha^{eq}(E)$ given by

$$\alpha^{eq}(E) = n_{opt}f(E)[1 - f(E + \hbar\,\omega_{LO})]D(E). \quad (11)$$

It corresponds to the first term of the series expansion of α as a function of the voltage V. Expressing the Fermi-Dirac functions, $\gamma(E)$ is simplified into

$$\gamma(E) = \exp\left(\frac{E_F^B - E_F^A}{k_bT}\right) = \exp\left(\frac{-qV}{k_bT}\right), \quad (12)$$

where T is the temperature of the sample and k_b the Boltzman constant.

We recall that in the context of infrared photovoltaic detection, applied biases are very small. The Johnson noise is related to the resistance at $0V$: R_0. In this calculation, it is then justified to linearize

$$1 - \gamma(E) \approx \frac{q}{k_bT}V. \quad (13)$$

This leads directly to the linear $I(V)$ behavior of the structure at low bias, through the multiplication by the constant α^{eq} (calculated with no applied voltage). For little variations of the voltage, the difference can be approximated by the following equation:

$$G_{ij}^{a}(V) - G_{ji}^{e}(V) \approx \int_{\epsilon_j - \hbar\omega_{LO}}^{+\infty} S_{ij}^{a}(E)\alpha^{eq}\frac{qV}{k_bT}dE \quad (14)$$

$$\approx G_{ij}^{a}(V = 0V)\frac{qV}{k_bT}. \quad (15)$$

A similar expression can be found for the difference

$$G_{ij}^{e}(V) - G_{ji}^{a}(V) \approx G_{ij}^{e}(V = 0V)\frac{qV}{k_bT}. \quad (16)$$

Finally, global current density is so evaluated by the formula

$$J = q\sum_{i \in A}\sum_{j \in B} G_{ij}\frac{qV}{k_bT}, \quad (17)$$

where the term G_{ij} is defined by the sum of G_{ij}^{a} and G_{ij}^{e} calculated without any applied voltage. R_0A can be finally deduced from the last equation,

$$R_0A = \frac{k_bT}{q^2\sum_{i \in A}\sum_{j \in B} G_{ij}}. \quad (18)$$

We have previously made the hypothesis that the electronic wave functions and the matrix elements are not depen-
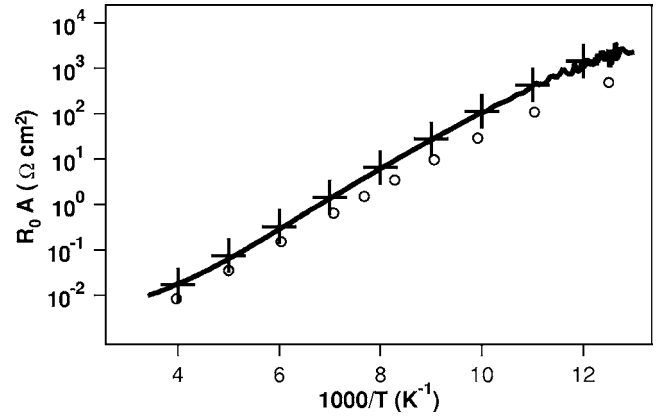

FIG. 5. R_0A as a function of $1000/T$, where T is the temperature of the sample. Solid line corresponds to the experimental curve. The circled-markers (respectively: the cross markers) are the results of the presented model considering a doping density of 5×10^{11} cm^{-2} (respectively 3×10^{11} cm^{-2}).

dent on the small bias. The current has been calculated as a result from a variation of the distribution of carriers as a function of the energy from cascade A to cascade B. This means that the current appears as a diffusion current, in a system with a nonhomogenous chemical potential. In this context, it is expected to find an expression of the R_0A which looks like an Einstein relation. By an identification between R_0A and $l^2/(qn_{2D}\mu)$ (where l is the period of the structure, n_{2D} is the 2D density, and μ is the electron mobility), we find indeed again $D/\mu = k_bT/q$, with the diffusion coefficient D expressed classically as a function of the transfer rates at equilibrium G_{ij} by

$$D = \frac{l^2\sum_{i \in A}\sum_{j \in B} G_{ij}}{n_{2D}}. \quad (19)$$

We find again $D = l^2/\tau$ used in the context of diffusion currents in p-n junctions.[17] It is remarkable in Eq. (18) that the R_0A can be calculated in a structure with no applied bias, considering only the transition rates G_{ij} at equilibrium, from one cascade to the next. Equation (18) appears as the main result of this paper. We have shown that the electronic transport in a complex structure as a QCD can be simplified. The transport is entirely dominated by two or three matrix elements present in the sum in Eq. (18), which is interpreted as an Einstein relation adapted to QCDs.

Figure 5 presents a typical example chosen to illustrate the quality of the modeling: the experimental R_0A of the device as a function of $1000/T$, where T is the temperature of the sample, and the result of our modeling using the previous Eq. (18) for two doping densities (5×10^{11} cm^{-2}, which corresponds to the nominal Si-donors concentration and 3×10^{11} cm^{-2}, which provides the best fit). Activation energy deduced from experimental curves lies around 120 meV. This energy corresponds to the transition between the first energy level E_1 and the energy level E_6. Dark current originates essentially from electrons transferred from level E_1 to level E_6, which is in an excelent agreement with the evaluation of the transfer rates presented in this article. The

theoretical modeling provides a good fit of the experimental curve: activation energy deduced from the model lies around 120 meV, too.

The resistivity given by the model considering the nominal doping density (5×10^{11} cm^{-2}) is slightly lower than the experimental value. We atribute this small discrepancy to a doping level slightly lower than expected. Indeed, including the lower doping level (3×10^{11} cm^{-2}) in the model provides a perfect fit of the experimental result, as shown in Fig. 5, and, on the other hand, the measurement of the integrated absorption agrees very well with this value of the doping level. Other small discrepancies between the experimental results and our model could come from other deviations of the structure parameters from the nominal values. The influence of the variations of structure parameters on the resistivity will be systematically reported in a forthcoming study. This is indeed necessary to analyze the performances of QCD focal plane arrays, in term of homogeneity.

V. CONCLUSION

In conclusion, we have reported a model of electronic transfers in a multiple quantum well device. Lifetimes associated with all transitions between two subbands are evaluated by considering only interactions between electrons and optical phonons. The resistivity of such a structure around a null bias voltage can then be deduced by Eq. (18), which appears as an Einstein relation. An excellent agreement is found between experimental result and our model, which does not include any other adjustable parameter than the doping density.

ACKNOWLEDGMENTS

*Present address: Laboratoire Kastler Brossel, Ecole normale supérieure, 24 rue Lhomond, 75005 Paris, France.

[1] H. Schneider and H. C. Liu, *Quantum Well Infrared Photodetector* (Springer, Berlin, 2006).

[2] L. Gendron, M. Carras, A. Huynh, V. Ortiz, C. Koeniguer, and V. Berger, Appl. Phys. Lett. **85**, 2824 (2004).

[3] M. Graf, G. Scalari, D. Hofstetter, J. Faist, H. Beere, E. Linfield, D. Ritchie, and G. Davies, Appl. Phys. Lett. **84**, 475 (2004).

[4] L. Gendron, C. Koeniguer, V. Berger, and X. Marcadet, Appl. Phys. Lett. **86**, 121116 (2005).

[5] J. A. Brum and G. Bastard, Phys. Rev. B **33**, 1420 (1986).

[6] J. A. Brum, T. Weil, J. Nagle, and B. Vinter, Phys. Rev. B **34**, 2381 (1986).

[7] E. Rosencher, B. Vinter, F. Luc, L. Thibaudeau, P. Bois, and J. Nagle, IEEE J. Quantum Electron. **30**, 2875 (1994).

[8] H. C. Liu, Appl. Phys. Lett. **60**, 1507 (1992).

[9] R. Koehler *et al.*, Nature (London) **417**, 156 (2002).

[10] J. Radovanović, V. Milanović, Z. Ilkonić, D. Indjin, and P. Harrison, J. Appl. Phys. **97**, 103109 (2005).

[11] A. Leuliet, A. Vasanelli, A. Wade, G. Fedorov, D. Smirnov, G. Bastard, and C. Sirtori, Phys. Rev. B **73**, 085311 (2006).

[12] S. M. Goodnick and P. Lugli, Phys. Rev. B **37**, 2578 (1988).

[13] P. Harrison, Appl. Phys. Lett. **75**, 2800 (1999).

[14] K. Kempa, Y. Zhou, J. R. Engelbrecht, and P. Bakshi, Phys. Rev. B **68**, 085302 (2003).

[15] K. Kempa *et al.*, Phys. Rev. Lett. **88**, 226803 (2002).

[16] R. Ferreira and G. Bastard, Phys. Rev. B **40**, 1074 (1989).

[17] E. Rosencher and B. Vinter, *Optoelectronics* (Cambridge University Press, Cambridge, England, 2002).